

ASYMMETRIC BEHAVIOR OF $H\alpha$ FOOTPOINT EMISSION DURING THE EARLY PHASE OF AN IMPULSIVE FLARE

JIONG QIU,¹ MING D. DING,² HAIMIN WANG,¹ PETER T. GALLAGHER,¹ JUN SATO,³
CARSTEN DENKER,¹ AND PHILIP R. GOODE¹

Received 2000 December 15; accepted 2001 February 1

ABSTRACT

We study the impulsive phase of a C9.0 solar flare using high temporal and spatial resolution $H\alpha$ images from Big Bear Solar Observatory (BBSO) in conjunction with high-cadence hard X-ray (HXR) observations from *Yohkoh*. During the early impulsive phase, HXR emission emerged from two kernels K1 and K2 which were connected by coronal loops observed in soft X-ray (SXR) images from *Yohkoh*. In $H\alpha$, the initial rise was observed in one flare kernel K2, which was followed within 10 s by enhanced emission in the associated kernel K1. Such a significant asymmetry was not observed at HXR wavelengths. Our analysis shows that the asymmetric $H\alpha$ footpoint emission cannot be explained by the magnetic mirroring effect in which strong field footpoints show lower precipitation rates. Instead, we study this phenomenon by investigating the atmospheric response of the lower chromosphere to nonthermal beam heating. From numerical simulations, it is suggested that a cool atmosphere does not respond rapidly to beam impact, which may explain the missing $H\alpha$ emission at K1 during the early impulsive phase. At K2, the early-phase atmosphere may be preferentially heated resulting in the $H\alpha$ emission rapidly following the HXR emission. This is due to the fact that K2 is a compact source which received persistent energy deposition and consequent heating in a confined area during the early phase. K1, on the other hand, is a diffused source which therefore experienced a lower heating rate per unity area. We propose a scenario in which the flare loop consists of multiple magnetic “threads” connecting the compact footpoint K2 with the diffuse footpoint K1.

Subject headings: Sun: activity — Sun: flares — Sun: magnetic fields

1. INTRODUCTION

It is well accepted that HXR emission in the impulsive phase of solar flares is largely produced at the footpoints of flare loops by energy exchange between hydrogen atoms and nonthermal electrons which are stopped at the upper chromosphere via Coulomb collision (Brown 1971). The impact of nonthermal electron beams gives rise to the excitation of hydrogen atoms and produces enhanced $H\alpha$ emission. Increased emission in the $H\alpha$ line wings can be produced when the dense lower chromosphere is sufficiently ionized by the penetrating electron beams. The physical process of heating, excitation, and ionization of the chromosphere by nonthermal beams takes place on a very short timescale (≤ 1 s), so it has been believed that high temporal and spatial resolution $H\alpha$ observations can be used to trace the temporal variations and spatial locations of nonthermal electrons during the impulsive phase.

In the case of nonthermal beam heating, the $H\alpha$ emission depends on the energy flux and power spectrum of the nonthermal electrons, and so $H\alpha$ observations allow us to retrieve information on the nonthermal electron population. However, $H\alpha$ emission produced by nonthermal beam heating also involves complicated radiative transfer processes. Accurate diagnostics of the emission requires sufficient understanding of the atmospheric response to the precipitated beams. Based on the numerical simulations of

the flare atmosphere dynamics (e.g., Fisher, Canfield, & McClymont 1985a, 1985b), Canfield & Gayley (1987) and Gayley & Canfield (1991) gave detailed theoretical analyses of the increased emission in the wings of the hydrogen Balmer lines. Their studies offer a guideline to understanding $H\alpha$ emission in terms of beam heating.

Since the 1980s, high-cadence campaigns have been conducted to investigate the fine-scale temporal structures of HXR and $H\alpha$ emission (Kiplinger et al. 1983; Neidig et al. 1993; Trotter et al. 2000; Wang et al. 2000). These observational results have confirmed the similarity between $H\alpha$ and HXR emission during the impulsive phase of solar flares to within the limit of their temporal resolution. Wang et al. (2000) also found that during the early impulsive phase, the rise of $H\alpha - 1.3 \text{ \AA}$ emission was delayed by several seconds with respect to the HXR bursts. They explained this as being a result of the long ionization timescale of the initially cool atmosphere. However, this issue was not fully addressed in their paper because of incomplete data coverage. In this paper, we analyze high-cadence observations of an impulsive C9.0 flare for which a complete data set was obtained. We specifically investigate $H\alpha$ and HXR emission in the early phase of the flare in order to understand the physics of nonthermal electron precipitation and heating of the lower atmosphere during this stage.

2. OBSERVATIONS

We conducted high-cadence flare observations at BBSO using a high frame rate Silicon Mountain Design 1M-60 camera. On 2000 March 16, we observed a C9.0 flare in NOAA AR8906 ($S16^\circ W31^\circ$) with a cadence of about 0.1 s at $H\alpha - 1.3 \text{ \AA}$. The pixel size of the CCD was $0''.36 \text{ pixel}^{-1}$. The image resolution was seeing limited, the measurable size in the best seeing condition being $0''.7$. During the 40

¹ Big Bear Solar Observatory, New Jersey Institute of Technology, 40386 North Shore Lane, Big Bear City, CA 92314-9672; qiu@bbso.njit.edu.

² Department of Astronomy, Nanjing University, 22 Hankou Road, Nanjing, Jiangsu 210093, China.

³ National Research Council, NASA Goddard Space Flight Center, Branch 682, Greenbelt, MD 20771.

minutes of continuous observations, the seeing was relatively stable. We first aligned the images rigidly with a cross-correlation algorithm, and then used a “destretching” algorithm to minimize image distortion due to seeing effects which cause differential motions of the features in an image. The accuracy in the co-alignment was better than $1''$. Each image was then normalized to the quiet-Sun intensity.

We also obtained *Yohkoh* data during the impulsive phase. These observations include SXR images from the Soft X-ray Telescope (SXT) and HXR data from the Hard X-ray Telescope (HXT) and Wide Band Spectrometer (WBS). The HXT is a Fourier synthesis imager, which observed the flare impulsive phase in four energy channels, L, M1, M2, and H (14–23–33–53–93 keV). From the HXT observations, we reconstructed HXR images using a modified maximum entropy method (MEM; Sakao 1994) with the improved calibration pattern of Sato et al. (1999). The *Transition Region and Corona Explorer (TRACE)* also observed the flare in high-cadence mode in UV 1600 Å continuum, while magnetograms of the longitudinal magnetic field were obtained using the Michelson Doppler Imager (MDI).

The HXR images were co-aligned with SXR images (Masuda 1994), and then further co-aligned with *TRACE* UV images using the pointing information of the two instruments. $H\alpha$ images from BBSO were also co-aligned with *TRACE* images to an accuracy of better than $1''$ by registering common features.

3. RESULTS

This flare was an impulsive event with the $H\alpha - 1.3 \text{ \AA}$ emission lasting for 3 minutes. As shown in Figure 1, we observed two bright kernels K1 and K2. In the MDI mag-

netogram (Fig. 2) observed a few minutes before the flare, K1 was located in a light bridge dividing a large negative spot into two parts, and K2 was within a positive magnetic pore. These two kernels were connected by SXR loop structure which was revealed in the SXT images (Fig. 2, panel c), thus they were most probably the conjugate footpoints of a flare loop. Figure 3 illustrates time profiles of the flare at various wavelengths. The $H\alpha$ intensity I in each kernel was obtained by taking the mean of the emission above the 85% contour level, I_0 indicating the preflare intensity. In this figure, the $H\alpha$ light curves show an intensity increase with respect to the preflare level. The two flare kernels have similar temporal evolution profiles, their temporal correlation coefficient being $\sim 90\%$. The HXR light curves all exhibit two major peaks, which can also be seen in $H\alpha$. The temporal correlation between the HXR flux in the L and M1 channels and the integrated $H\alpha$ emission from the overall flare region is greater than 80%. The simultaneity of the HXR and the $H\alpha$ emission in both kernels can be understood as being a result of electrons simultaneously precipitating and losing their energy at the flare loop footpoints.

We note one distinct phenomenon observed during the early impulsive phase, that is, K2 exhibited enhanced $H\alpha$ and HXR emission, while K1 showed no significant $H\alpha$ emission for about 10 s. Since K2 was located in one magnetic polarity, it is unlikely that the initial energy release occurred only at a single polarity footpoint of the flare loop. With high-resolution images, we identified the early rise of $H\alpha$ in K2 which is located within a small area of positive polarity (Fig. 2). Clearly, this confined region represents the location into which electrons were deposited at the start of the flare. During this episode, the location and size of the initial brightening did not vary significantly, the FWHM of

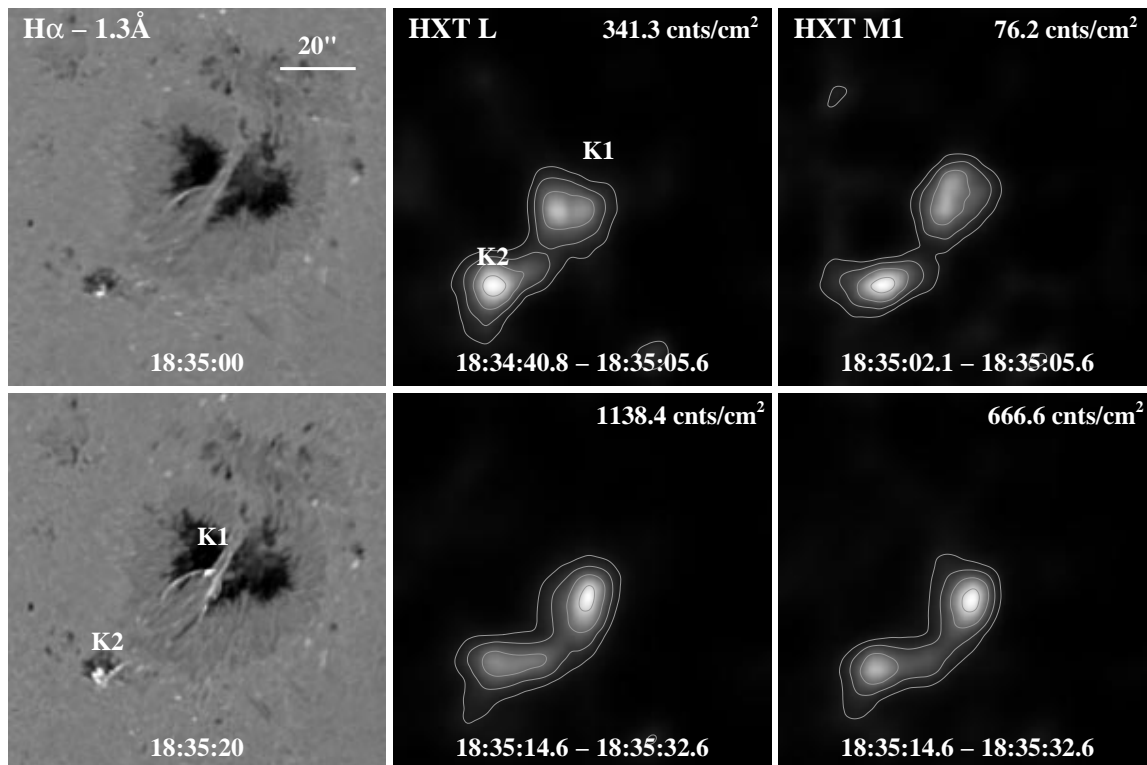


FIG. 1.—Early phase of the flare observed at $H\alpha - 1.3 \text{ \AA}$ (left panel), and in the HXR L (middle panel) and M1 (right panel) channels. The images at $H\alpha - 1.3 \text{ \AA}$ are shown in a logarithmic scale to demonstrate both bright and weak features.

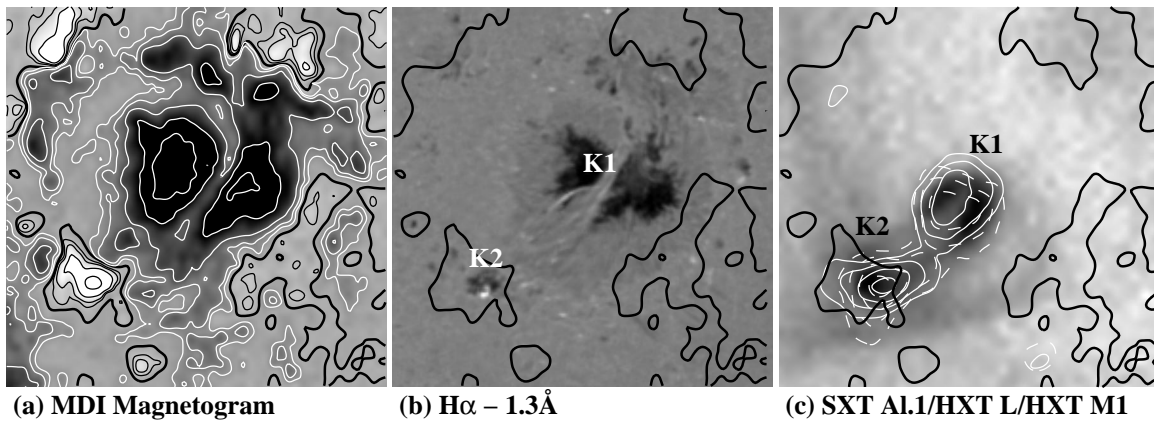


FIG. 2.—(a) MDI magnetogram at 18:27 UT. The white/dark contours indicate the negative/positive magnetic fields, the contour levels being $\pm 100, 200, 400, 800,$ and 1200 G. (b) H α $- 1.3 \text{ \AA}$ filtergram at 18:35:00 UT, showing the early phase of the flare. (c) SXR image from the *Yohkoh*/SXT Al.1 filter at 18:35:14 UT superposed with HXR contours from the *Yohkoh*/HXT L (thin solid line) and M1 (thin dashed line) channels. The HXR emission in the L and M1 channels is integrated from 18:34:40 to 18:35:05 UT, and from 18:35:02 to 18:35:05 UT, respectively, the contour levels being 0.1, 0.2, 0.4, and 0.8 of the maximum. In all three figures, the thick solid lines indicate the inversion lines of the longitudinal magnetic field.

the brightened area being $1''.71 \pm 0''.16$. K1, on the other hand, did not exhibit significant enhancement during the early phase. We estimate that the contrast increase, $I - I_0$, in K2 was about an order of magnitude greater than in K1.

The H α behavior in the early phase indicates either unequal nonthermal energy deposition or asymmetric footpoint heating, or possibly a combination of both. Unequal nonthermal energy deposition has previously been reported in spatially resolved HXR observations by Sakao (1994), Li et al. (1997), Kundu et al. (1995), and Wang et al. (1996), and can be interpreted as being a result of magnetic mirroring, where the brighter HXR footpoint is located in the weaker magnetic field. According to Melrose & White (1981), $R_1/R_2 = B_2/B_1$, where R_1 and R_2 are the precipitation rates at the two footpoints, and B_1 and B_2 are the magnetic field strength. From the MDI magnetogram we find that the magnetic field strength was ~ 800 G at K1 and 500 G at K2, thus giving a ratio R_1/R_2 of ~ 0.6 . However, considering that K1 was located in a light bridge which receives certain scattered light from the sunspot in a magnetogram, the real magnetic field strength in K1 must be weaker than 800 G. By the same measure, because of the scattered light from the surrounding quiet-Sun region, B_2 may be underestimated. As a result, the real ratio R_1/R_2 should be close to unity. To examine the nonthermal energy deposition, we reconstructed the HXR images in the L and M1 channels during the early phase of the flare. Figure 2, panel c, shows the HXR emission in the L channel integrated from 18:34:40 to 18:35:05 UT, together with that in the M1 channel which was integrated from 18:35:02 to 18:35:05 UT. The *Yohkoh* HXT flare mode was switched on at 18:35:02 UT, hence, information before this time was not obtained from the HXT M1-H channels. There are not sufficient data counts to construct images in M2 and H channels during this period. The HXR emission emerged from two sites coincident with the H α kernels K1 and K2, and the ratio of the precipitation rates (in units of counts s^{-1}) at the two kernels is estimated to be ~ 0.8 – 0.9 in the L and M1 channels. These values are consistent with those predicted by the mirroring effect.

We can also use H α $- 1.3 \text{ \AA}$ emission as a proxy for non-thermal electrons (Canfield & Gayley 1987; Canfield et al. 1993). The residual specific intensity, $\Delta I = I - I_0$, where I_0

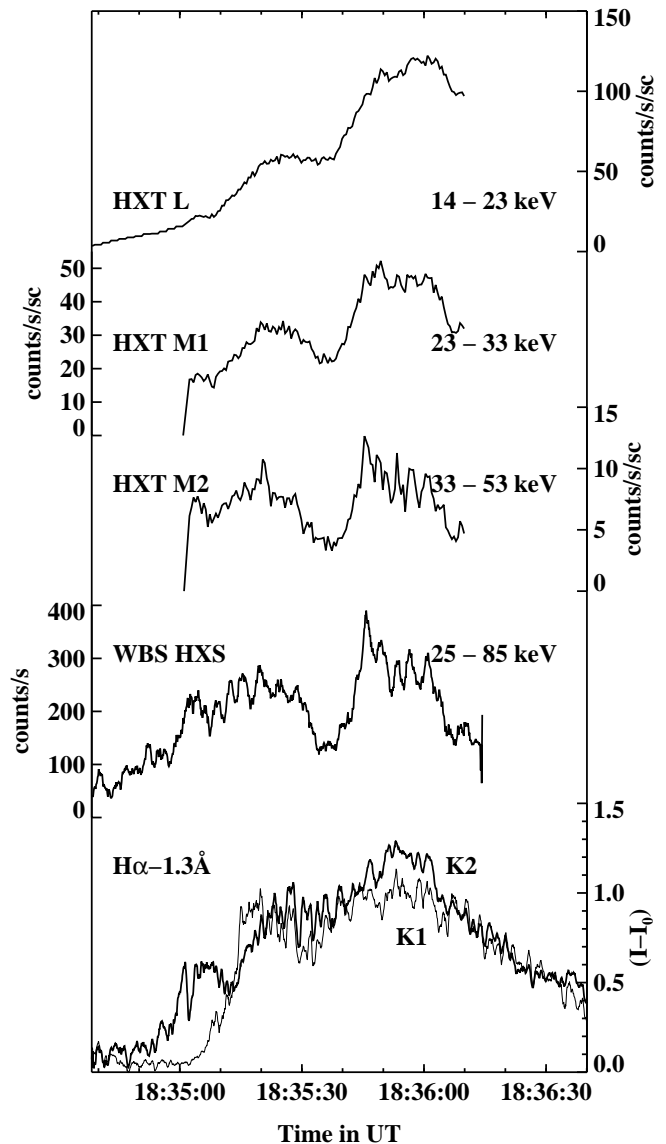


FIG. 3.—HXR and H α time profiles of the flare. In the bottom panel, the thick and thin solid lines indicate H α intensity from K2 and K1, respectively; I_0 is the preflare intensity.

is the preflare intensity, in the H α far wing is optically thin and is roughly proportional to the opacity of the beam heated chromosphere. From Canfield & Gayley (1987), the H α intensity is related to the nonthermal influx in the following way, $\Delta I/I_c = [N_c/H]q^{4/(\delta+2)}G(\delta)K$, where I_c is the continuum intensity, δ is the power-law index of the nonthermal beam, N_c is the stopping depth determined by the lower energy cutoff E_c , H is the preflare scale height, q is the beam strength parameter measuring the characteristic heating per hydrogen nucleus relative to 10^{-9} ergs s^{-1} , $G(\delta)$ is a function of δ , and K is a coefficient decided by the characteristic temperature T and ionization x , and is rather insensitive to the beam parameters. Assuming the nonthermal electron beams precipitated at the two footpoints have the same power spectrum and energy cutoff, the ratio of the H α footpoint intensities is scaled as $\Delta I_1/\Delta I_2 = (q_1/q_2)^{4/(\delta+2)}$. From 18:35:02 to 18:35:05 UT, the ratio of the HXR flux in the M1 channel to that in the L channel is ~ 0.8 , yielding an electron beam power-law index of ~ 4.4 . This indicates that the HXR emission during this early phase is basically nonthermal. The ratio of the beam intensity at the two kernels is given by $q_1/q_2 = (R_1/S_1)/(R_2/S_2)$, where S_1 and S_2 are the HXR source areas in K1 and K2, respectively. S_1 and S_2 are measured as the area encompassed by the 25% contours of the maximum counts in each kernel in HXR images. If we measure S_1 and S_2 in the HXR image in the L channel, $\Delta I_1/\Delta I_2 \sim 0.7$; if S_1 and S_2 are measured in the M1 channel, $\Delta I_1/\Delta I_2 \sim 0.6$. These values are still significantly larger than those of the H α observations. It should be noted that the HXT image resolution is in the order of $5''-10''$, so there is a large uncertainty in the above estimate. Nevertheless, we can still say that the magnetic mirroring effect is not able to explain the missing H α emission in K1, because such an explanation requires that the actual electron precipitation area in K1 has to be much greater than in K2 by an order of magnitude, which is unlikely judging from both HXT and H α observations.

4. PARAMETRIC ANALYSIS

From above, the relative contrast in the H α blue wing is determined by a few physical parameters. These parameters can be studied in two groups: those describing the beam properties, i.e., nonthermal beam strength q , spectral index δ , and cutoff energy E_c , and those describing the atmosphere and its response to nonthermal beam impact, namely, the preflare scale height H , temperature T , electron density n_e , and fractional ionization x . The parameters in the latter group are not independent of each other nor of the beam parameters, and any investigation of the atmospheric response must be handled by numerically solving the radiative transfer equations.

Assuming the preflare atmospheric conditions in the two locations are the same, we can study the H α emission due to changing nonthermal beam properties. Figure 4a illustrates the ratio of the H α contrast increase at the two kernels as a function of q_1/q_2 for varying values of δ . From this figure, it is apparent that, with the same spectral index δ , a small difference in beam strength q , as supported by the HXR observations in this event, cannot result in a large difference in ΔI , and therefore, the missing emission at K1. This figure also shows that for larger values of q_1/q_2 , $\Delta I_1/\Delta I_2$ is not particularly sensitive to the power-law index δ .

The nonthermal beam flux (ergs s^{-1} cm^{-2}) is determined by both the beam strength q and the energy cutoff E_c via

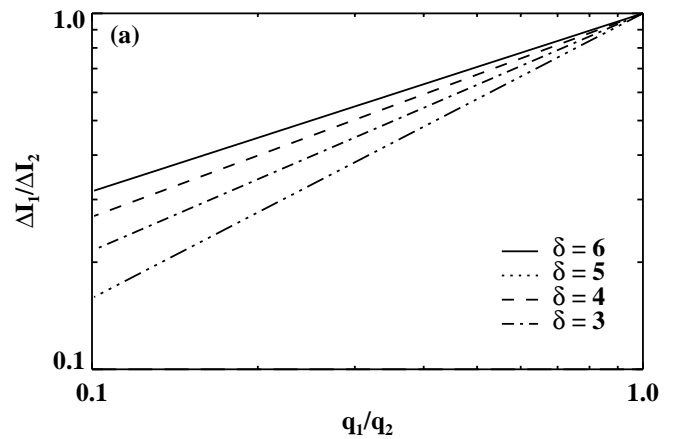


FIG. 4a

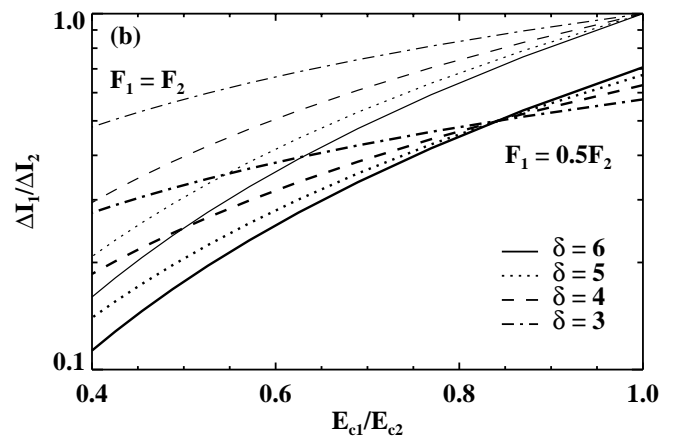


FIG. 4b

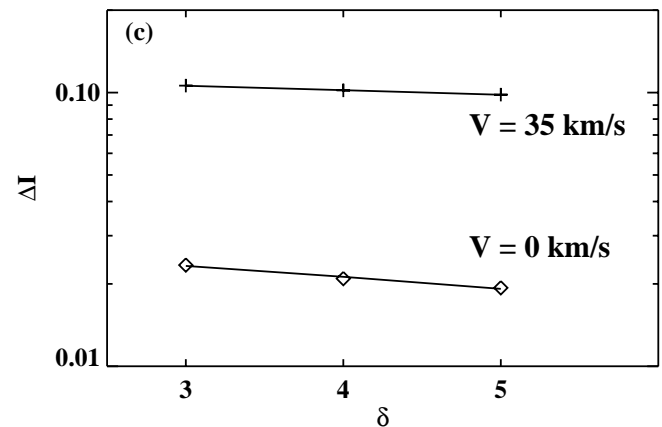


FIG. 4c

FIG. 4.—(a) plot of $\Delta I_1/\Delta I_2$ as a function of q_1/q_2 at varying values of δ . (b) $\Delta I_1/\Delta I_2$ as a function of E_{c1}/E_{c2} at varying values of δ , in the case of $F_1 = F_2$ (thin lines) and $F_1 = 0.5F_2$ (thick lines). (c) ΔI as a function of δ with or without a macro-turbulence velocity V .

$F \sim qE_c^2$. We investigate the case where the nonthermal energy cutoff differs at the two kernels as illustrated in Figure 4b. It is shown that in either of the two considered cases, $F_1 = F_2$ and $F_1 = 0.5F_2$, the cutoff energy in K2 must be at least twice that of K1, i.e., $E_{c1}/E_{c2} \sim 0.5$, to produce the observed H α emission difference between the two kernels. This is not impossible, but the reason for the very different E_c in the two kernels is not clear.

We also consider various situations in which $\delta_1 \neq \delta_2$. Figure 4c illustrates the results of ΔI at H α – 1.3 Å versus δ which were obtained from non-LTE numerical simulations. The simulation takes the flare model F1 of Machado et al. (1980) as the preflare model atmosphere, and solves the level population equation and radiative transfer equation for hydrogen Balmer lines under nonthermal electron beam impact. In the simulation, the cutoff energy is taken as 20 keV, and the nonthermal energy flux is 10^9 ergs cm $^{-2}$ s $^{-1}$. Figure 4c shows that ΔI is not sensitive to the change in δ . Therefore, given the similar nonthermal flux and energy cutoff, a possible difference in δ is not an important factor in producing a large difference in ΔI between the two kernels.

It was shown by Wang et al. (2000) that flares may contain a large number of small-scale, short-lived elementary bursts, which are thought to be produced by consecutive or overlapping electron beam pulses. In this case, both the HXR and H α emissions are actually a superposition of numerous spatially and temporally unresolved pulses. The numerical simulations of M. D. Ding, J. Qiu, & H. Wang (2000, in preparation) suggest that the amplitude of H α emission relies on the heating status of the preflare atmosphere. The same electron beam pulse is likely to produce greater H α fluctuation with a heated background atmosphere. Ding et al. (2001) also show that the H α wing emission can be significantly enhanced by introducing a large macroturbulence. This effect is illustrated in Figure 4c. A sufficiently large macrovelocity (e.g., $V \sim 35$ km s $^{-1}$) can Doppler-shift the core emission to the line wings, increasing the wing emission by nearly an order of magnitude. The physical meaning of macroturbulence is still poorly understood, but it is believed to be related to the heating and dynamics of the solar atmosphere.

We therefore propose a possible explanation of the missing H α emission at K1. If during the early phase of the flare, the background atmosphere of K1 is relatively cool, and the macroturbulence, as related to the extent of heating and dynamics, is small, then the H α wing emission in K1 would be less enhanced relative to K2. It is difficult to determine the cause of such a scenario. Nevertheless, from a morphological point of view, K2 is a compact source, while

K1 is diffuse. It is likely that the magnetic loop connecting K1 and K2 is a bundle of fine magnetic “threads,” with one end concentrated at K2 and the other end scattered around K1, as illustrated in Figure 5. In such a configuration, it is expected that persistent and concentrated heating at K2 can efficiently raise the temperature and induce turbulence in the lower atmosphere, while at K1, nonthermal electrons precipitate along the magnetic “threads” in a diffused area, which does not produce persistent heating at a single site inside K1. As a result, the atmosphere at K1 remains cool in the early phase of the flare until 10 s later when much stronger nonthermal beam precipitation and therefore heating sets in. This picture also suggests that the magnetic flux in the K1 region is highly fragmented, as is the flare loop. Observationally, such aggregation of the fine-scale “threads” cannot yet be confirmed because of the lack of sufficient resolution.

5. CONCLUSION

Temporally and spatially resolved ground-based and satellite observations often reveal a close correlation between HXR and H α emission during the impulsive phase of solar flares, which offers a clue to the physical process of energy release and heating of the lower atmosphere by nonthermal beams during the early phase of flares. In this paper, through comparisons of high temporal and spatial resolution H α and HXR observations of a C9.0 flare, we find that such a correlation is not always present. During the initial stage of the flare, the event studied exhibits significant H α emission in only one footpoint of the flare loop, although HXR emission emerges from both footpoints. We investigate the cause for the missing H α emission in the other footpoint and suggest that the atmosphere at this location may be relatively cool, so that the atmospheric response to nonthermal beams is slow, the H α emission therefore showing a delay. This can be supported by numerically solving the radiative transfer equations for the lower atmosphere in response to nonthermal electron precipitation (M. D. Ding et al. 2000, in preparation). According to the morphology of the two footpoints, it is very likely that the footpoint that produces HXR correlated H α emission is a compact source allowing persistent precipitation

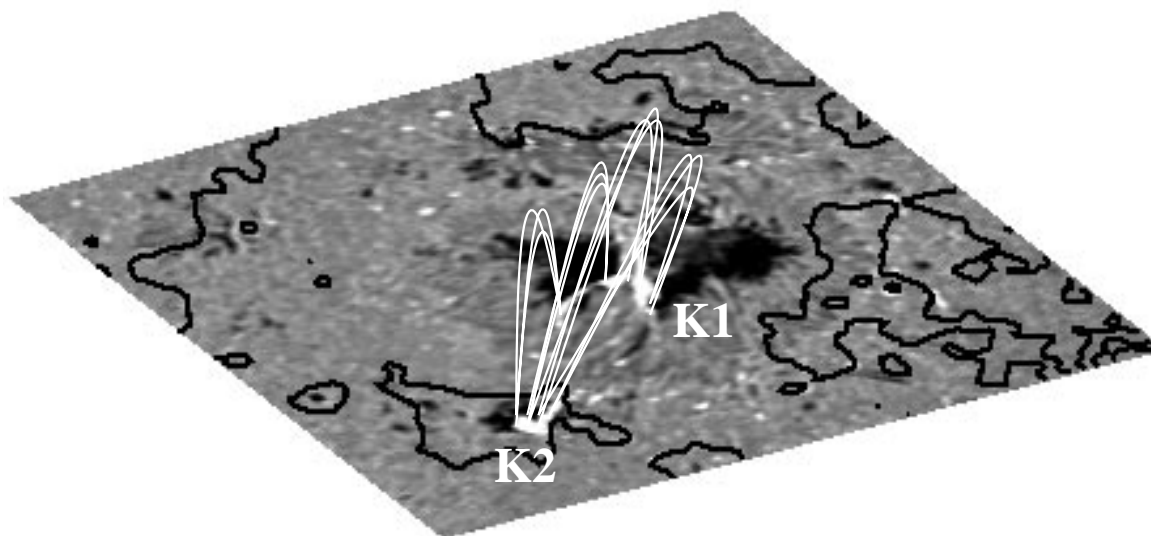


FIG. 5.—Sketch of the magnetic configuration of the flare illustrating multiple magnetic “threads” connecting the two footpoints K1 and K2. The image shows the H α – 1.3 Å filtergram at 18:35:27 UT, and the dark solid lines indicate the magnetic inversion lines.

and heating during the early phase of the flare, while the footpoint lacking $H\alpha$ emission is a diffuse source with non-thermal electrons scattered in a more extended area, so that the average temperature of the atmosphere is low. Such a scenario indicates that the magnetic loop connecting the two footpoints consists of fine magnetic “threads” whose ends are concentrated in one kernel and scattered in the other kernel.

The authors thank H. Hudson for offering *Yohkoh* data and BBSO observing staff and TRACE team for data support. We thank the referee for helping improve the paper. This work is supported by NSF under grants ATM-9714796 and ATM-0076602, NASA under grants NAG5-9682, NAG5-7837, NAG5-9543, and NAG5-9501, and ONR under grant N00014-97-1-1037.

REFERENCES

- Brown, J. C. 1971, *Sol. Phys.*, 18, 489
 Canfield, R. C., et al. 1993, *ApJ*, 411, 362
 Canfield, R. C., & Gayley, K. G. 1987, *ApJ*, 322, 999
 Ding, M. D., Qiu, J., Wang, H., & Goode, P. R. 2001, *ApJ*, 552, 340
 Fisher, G. H., Canfield, R. C., & McClymont, A. N. 1985a, *ApJ*, 289, 425
 ———. 1985b, *ApJ*, 289, 434
 Gayley, K. G., & Canfield, R. C. 1991, *ApJ*, 380, 660
 Kiplinger, A. L., Dennis, B. R., Emslie, A. G., Frost, K. L., & Orwig, L. E. 1983, *ApJ*, 265, L99
 Kundu, M. R., Nitta, N., White, S. M., Shibasaki, K., Enome, S., Sakao, T., Kosugi, T., & Sakurai, T. 1995, *ApJ*, 454, 522
 Li, J., Metcalf, T. R., Canfield, R. C., Wuelser, J.-P., & Kosugi, T. 1997, *ApJ*, 482, 490
 Machado, M. E., Avrett, E. H., Vernazza, J. E., & Noyes, R. W. 1980, *ApJ*, 242, 336
 Masuda, S. 1994, Ph.D. thesis, Univ. Tokyo
 Melrose, D. B., & White, S. M. 1981, *J. Geophys. Res.*, 86, 2183
 Neidig, D. F., Kiplinger, A. L., Cohl, H. S., & Wiborg, P. H. 1993, *ApJ*, 406, 306
 Sakao, T. 1994, Ph.D. thesis, Univ. Tokyo
 Sato, J., Kosugi, T., & Makishima, K. 1999, *PASJ*, 51, 127
 Trotter, G., Rolli, E., Magun, A., Barat, C., Kuznetsov, A., Sunyaev, R., & Terekhov, O. 2000, *A&A*, 356, 1067
 Wang, H., Gary, D. E., Zirin, H., Nitta, N., Schwartz, R. A., & Kosugi, T. 1996, *ApJ*, 456, 403
 Wang, H., Qiu, J., Denker, C., Spirock, T., Chen, H., & Goode, P. R. 2000, *ApJ*, 542, 1080